Extended finite elements for 3D–1D coupled problems via a PDE-constrained optimization approach

Finite Elements in Analysis and Design 239 (2024) 104203

Contents lists available at ScienceDirect

Finite Elements in Analysis & Design

journal homepage: www.elsevier.com/locate/finel

Extended finite elements for 3D–1D coupled problems via a PDE-constrained optimization approach

Denise Grappein [*,1], Stefano Scialò[1], Fabio Vicini[1]

Dipartimento di Scienze Matematiche, Politecnico di Torino, Corso Duca degli Abruzzi 24, 10129 Torino, Italy

ARTICLE INFO

MSC:
65N30
65N50
68U20

Keywords:
3D–1D coupled problems
Non conforming meshes
Extended finite elements
Numerical quadrature

ABSTRACT

In this work, we propose the application of the eXtended Finite Element Method (XFEM) in the context of the coupling between three-dimensional and one-dimensional elliptic problems. In particular, we consider the case in which the 3D–1D coupled problem arises from the geometrical model reduction of a fully three-dimensional problem, characterized by thin tubular inclusions embedded in a much wider domain. In the 3D–1D coupling framework, the use of non conforming meshes is widely adopted. However, since the inclusions typically behave as singular sinks or sources for the 3D problem, mesh adaptation near the embedded 1D domains may be necessary to enhance solution accuracy and recover optimal convergence rates. An alternative to mesh adaptation is represented by the XFEM, which we here propose to enhance the approximation capabilities of an optimization-based 3D–1D coupling approach. An effective quadrature strategy is devised to integrate the enrichment functions and numerical tests on single and multiple segments are proposed to demonstrate the effectiveness of the approach.

1. Introduction

The present work deals with coupled partial differential equation problems on 3D and 1D domains arising from the application of dimensional reduction models to equi-dimensional problems where cylindrical or nearly-cylindrical inclusions are embedded in a larger 3D domain, [1–3]. Other examples of coupled problems with non-zero dimensional gap, not considered in this work, are configurations where the lower dimensional domain is not embedded but is an extension of the higher dimensional one, as, e.g., in the coupling between bulk structures and fins or plates in elastodynamics [4], in 2D–1D hydrodynamics models [5], in heterogeneous rod models [6] or in cardiovascular simulations as the ones reviewed in [7].

The treatment of the smaller features of the domain as lower dimensional manifolds can reduce the overhead of simulations, and the cost related to the generation of a computational mesh. Here, narrow and elongated embedded inclusions are considered, dimensionally reduced to one-dimensional manifolds in the bulk three dimensional domain. Suitable matching conditions need to be added at the interfaces to close the problem, depending on the nature of the described physical phenomenon: in some cases the solution is expected to be continuous at the interface, as in the description of damaged vessels in tumour induced angiogenesis [8], of thin membranes [9], or in the modeling of fiber reinforced materials [10]; in other cases, filtration like conditions, yielding a discontinuity at the 3D–1D interfaces are preferred, as for plant-roots nutrient uptake from the subsoil [11,12], in geological applications [13], or again in angiogenesis [14,15]. However, the mathematical formulation of these 3D–1D coupled problems requires non-standard approaches, and specialized numerical schemes are needed to correctly account for the presence

* Corresponding author.
E-mail addresses: denise.grappein@polito.it (D. Grappein), stefano.scialo@polito.it (S. Scialò), fabio.vicini@polito.it (F. Vicini).
[1] Member of INdAM research group GNCS.

https://doi.org/10.1016/j.finel.2024.104203
Received 20 February 2024; Received in revised form 13 May 2024; Accepted 10 June 2024
Available online 24 June 2024

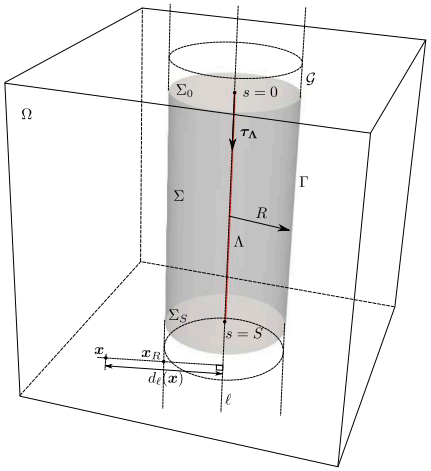

Fig. 1. Domain with single inclusion and description of notation. The size of the inclusion is exaggerated for description purposes.

of singularities. A possibility lies in the use of regularizing functions to approximate the singular terms [16,17], or of lifting techniques [1]. In [18] the solution is split in a regular part, approximated by standard methods, and an irregular part, for which an analytical solution is given. Domain decomposition approaches are finally proposed in [19] based on Lagrange multipliers, and in [3,20] where a PDE-constrained optimization method is presented.

The use of a 3D mesh non conforming to the 1D domains is quite standard. However, in some cases, sub-optimal convergence rates are observed unless adaptive refinement close to the singularity is used, see e.g. [15,16]. In this work we adopt the eXtended Finite Element Method (XFEM) [21] as an alternative to mesh refinement. The application of XFEM to 3D problems with singular sources has been proposed in [22], in particular for quasi 3D problems describing the effect of well leakage in aquifers. In [23] the methodology was extended to fully 3D–1D coupled problems in mixed formulation. The function space for the velocity variable is enriched, and non intersecting segments entirely crossing the computational domain are considered in the numerical examples.

Here, we focus on the application of the XFEM to enhance the approximation capabilities of the optimization-based 3D–1D coupling strategy proposed in [3,20]. Such method is based on a three-field domain decomposition strategy, in which additional interface variables are introduced to de-couple the problem on the inclusions from the problem in the bulk domain. A cost functional is introduced to measure the error in satisfying the desired matching condition at the interfaces, and minimized to recover a global solution. Different interface conditions are considered in [3] and in [20], resulting in two different formulations of the method. In the present work we consider flux conservation and pressure continuity at the interface as in [3]. However, the proposed approach can be easily extended to other interface conditions, such as the ones considered in [20], or even to different formulations of the problem. We enrich the function space of the 3D pressure variable with a globally continuous function, having a log-like behavior outside the inclusion and being constant inside it. The choice of the enrichment function is based on the results provided in [18], adapted to the present case. We suggest an ad-hoc quadrature scheme for the numerical integration of the resulting irregular basis functions. We consider intersecting/branching inclusions, possibly ending inside the domain.

The manuscript is organized as follows: the model problem is presented in Section 2, and an overview on the PDE-constrained optimization approach is provided in Section 3; Section 4 is devoted to the general discretization of the optimization problem, while the details on the application of the XFEM are provided in Section 5. In Section 6 we propose a quadrature strategy, suitably designed to integrate the enriched basis functions and finally, in Section 7, some numerical experiments are presented, in order to validate the proposed approach.

2. Notation and model problem

We consider a convex domain $\Omega \subset \mathbb{R}^3$, characterized by the presence of a thin cylindrical inclusion $\Sigma \subset \Omega$ of radius R, see Fig. 1. We assume R to be smaller than both the diameter of the domain and the length of the cylinder. The centerline of Σ is denoted by $\Lambda = \{\lambda(s),\ s \in (0, S)\}$, and $\boldsymbol{\tau}_{\boldsymbol{\Lambda}}$ is the unit tangent vector to Λ. We further call ℓ the line passing through the centerline of Σ and $\mathcal{G}$ the lateral surface of an infinite cylinder with centerline ℓ and radius R. The boundary of Ω is denoted by $\partial\Omega$ and is split into two subsets: the Dirichlet boundary $\partial\Omega_{\mathrm{d}}$ and the Neumann boundary $\partial\Omega_{\mathrm{n}}$, such that $\partial\Omega = \overline{\partial\Omega_{\mathrm{d}}} \cup \overline{\partial\Omega_{\mathrm{n}}}$, with $\partial\Omega_{\mathrm{d}} \cap \partial\Omega_{\mathrm{n}} = \emptyset$ and $|\partial\Omega_{\mathrm{d}}| > 0$. The boundary of Σ is split into the lateral surface Γ and the two end sections Σ_0 and Σ_S, i.e. $\partial\Sigma = \overline{\Gamma} \cup \overline{\Sigma_0} \cup \overline{\Sigma_S}$. The symbol $\Sigma(s)$, $s \in (0, S)$, is used to denote a generic cross-section of Σ. Finally, we define $D := \Omega \setminus \overline{\Sigma}$, the domain without the inclusion, having boundary $\partial D = \partial\Omega \cup \partial\Sigma$.

Let us now consider a diffusion problem in D and Σ with unknown pressures $u \in D$ and $\tilde{u} \in \Sigma$:

$$-\nabla \cdot (K \nabla u) = f \qquad \text{in } D \tag{1}$$

$$u_{|_\Gamma} = \psi \qquad \text{on } \Gamma \tag{2}$$
$$K\nabla u \cdot \boldsymbol{n} = \phi \qquad \text{on } \Gamma \tag{3}$$
$$u = 0 \qquad \text{on } \partial\Omega_{\mathrm{d}} \tag{4}$$
$$\nabla u \cdot \boldsymbol{n} = 0 \qquad \text{on } \partial\Omega_{\mathrm{n}} \tag{5}$$
$$\nabla u \cdot \boldsymbol{n} = 0 \qquad \text{on } \Sigma_0 \cup \Sigma_S \tag{6}$$

$$-\nabla \cdot (\tilde{K}\nabla\tilde{u}) = g \qquad \text{in } \Sigma \tag{7}$$
$$\tilde{u}_{|_\Gamma} = \psi \qquad \text{on } \Gamma \tag{8}$$
$$\tilde{K}\nabla\tilde{u} \cdot \tilde{\boldsymbol{n}} = -\phi \qquad \text{on } \Gamma \tag{9}$$
$$\nabla\tilde{u} \cdot \tilde{\boldsymbol{n}} = 0 \qquad \text{on } \Sigma_0 \cup \Sigma_S \tag{10}$$

The symbol ψ denotes the unknown unique value of the pressure on the interface Γ, whereas ϕ is the unknown flux through Γ, entering in D. For the sake of simplicity, we assume that all boundary conditions, except the interface conditions prescribed on Γ, are homogeneous. The vector $\boldsymbol{n}$ denotes the outward-pointing unit normal to ∂D, while $\tilde{\boldsymbol{n}} = -\boldsymbol{n}$ is the outward pointing unit normal to $\partial\Sigma$.

3. Optimization formulation for the 3D-1D reduced problem

Following [3], to which we refer for details, the above 3D–3D coupled problem is reformulated as a 3D–1D coupled problem through a suitable choice of function spaces for the solution. Given the small radius of the inclusion, the solution is assumed to be constant on its cross sections and their boundaries. Let us hence define two extension operators:

$$\mathcal{E}_{_\Sigma} : H^1(\Lambda) \to H^1(\Sigma) \quad \text{and} \quad \mathcal{E}_{_\Gamma} : H^1(\Lambda) \to H^{\frac{1}{2}}(\Gamma),$$

which, given a function $\hat{v} \in H^1(\Lambda)$, uniformly extend the value $\hat{v}(s)$, $s \in [0, S]$ to the cross section $\Sigma(s)$ of the cylinder, i.e. $\mathcal{E}_{_\Sigma}\hat{v}(\boldsymbol{x}) = \hat{v}(s)\ \forall \boldsymbol{x} \in \Sigma(s)$, and to the boundary $\Gamma(s)$ of $\Sigma(s)$, i.e. $\mathcal{E}_{_\Gamma}\hat{v}(\boldsymbol{x}) = \hat{v}(s)\ \forall \boldsymbol{x} \in \Gamma(s)$. Given the trace operator $\gamma_{_\Gamma} : H^1(D) \cup H^1(\Sigma) \to H^{\frac{1}{2}}(\Gamma)$, defined as $\gamma_{_\Gamma} v = v_{|_\Gamma}\ \forall v \in H^1(D) \cup H^1(\Sigma)$, and setting $\hat{V} = H^1(\Lambda)$, the following spaces are introduced:

$$\widetilde{V} = \{v \in H^1_0(\Sigma) : v = \mathcal{E}_{_\Sigma}\hat{v},\ \hat{v} \in \hat{V}\}, \quad \mathcal{H}^{\Gamma} = \{v \in H^{\frac{1}{2}}(\Gamma) : v = \mathcal{E}_{_\Gamma}\hat{v},\ \hat{v} \in \hat{V}\}$$

$$V_D = \left\{ v \in H^1(D) : v_{|_{\partial\Omega_{\mathrm{d}}}} = 0 \text{ and } \gamma_{_\Gamma} v \in \mathcal{H}^{\Gamma} \right\},$$

whose functions satisfy the hypothesis on the regularity of the solution. Denoting by $(\cdot,\cdot)_\star$ the L^2-scalar product on a generic domain $\star$, by X' the dual of a space X, and by $\langle\cdot,\cdot\rangle_{X',X}$ the duality pairing between the two spaces, the weak formulation of (1)–(10) reads: *find* $(u, \tilde{u}) \in V_D \times \widetilde{V}$, $\psi \in \mathcal{H}^{\Gamma}$, $\phi \in \mathcal{H}^{\Gamma\prime}$ *such that*

$$(K\nabla u, \nabla v)_D - \left\langle \phi, \gamma_{_\Gamma} v \right\rangle_{\mathcal{H}^{\Gamma\prime},\mathcal{H}^{\Gamma}} = (f, v)_D \qquad \forall v \in V_D, \tag{11}$$
$$(\tilde{K}\nabla\tilde{u}, \nabla\tilde{v})_\Sigma + \left\langle \phi, \gamma_{_\Gamma}\tilde{v} \right\rangle_{\mathcal{H}^{\Gamma\prime},\mathcal{H}^{\Gamma}} = (g, \tilde{v})_\Sigma \qquad \forall \tilde{v} \in \widetilde{V}, \tag{12}$$
$$\left\langle \gamma_{_\Gamma} u - \psi, \eta \right\rangle_{\mathcal{H}^{\Gamma},\mathcal{H}^{\Gamma\prime}} = 0 \qquad \forall \eta \in \mathcal{H}^{\Gamma\prime}, \tag{13}$$
$$\left\langle \gamma_{_\Gamma}\tilde{u} - \psi, \eta \right\rangle_{\mathcal{H}^{\Gamma},\mathcal{H}^{\Gamma\prime}} = 0 \qquad \forall \eta \in \mathcal{H}^{\Gamma\prime}. \tag{14}$$

A well posed 3D–1D formulation follows by operating a geometrical reduction of the operators:

$$\left\langle \phi, \gamma_{_\Gamma} v \right\rangle_{\mathcal{H}^{\Gamma\prime},\mathcal{H}^{\Gamma}} = \int_\Gamma \phi\ \gamma_{_\Gamma} v\ d\Gamma = \int_0^S \Big(\int_{\Gamma(s)} \phi\ \gamma_{_\Gamma} v\ dl \Big) ds =$$
$$= \int_0^S |\Gamma(s)| \overline{\phi}(s) \check{v}(s)\ ds = \left\langle |\Gamma| \overline{\phi}, \check{v} \right\rangle_{\hat{V}',\hat{V}} \qquad \forall v \in V_D,$$

$$(\tilde{K}\nabla\tilde{u}, \nabla\tilde{v})_\Sigma = \int_\Sigma \tilde{K}\nabla\tilde{u}\nabla\tilde{v}\ d\sigma = \int_0^S \tilde{K}|\Sigma(s)| \frac{d\hat{u}}{ds}\frac{d\hat{v}}{ds}\ ds,$$

where $\check{v} \in \hat{V}$ is such that $\gamma_{_\Gamma} v = \mathcal{E}_{_\Gamma}\check{v}$, and $\hat{u}, \hat{v} \in \hat{V}$ such that $\tilde{u} = \mathcal{E}_{_\Sigma}\hat{u}$, $\tilde{v} = \mathcal{E}_{_\Sigma}\hat{v}$. The quantities $|\Gamma(s)|$ and $|\Sigma(s)|$ are the measure of $\Gamma(s)$ and $\Sigma(s)$, respectively.

Instead of solving the coupled system of Eqs. (11)–(14), we re-write it as a PDE-constrained optimization problem. This is done by introducing a cost functional to measure the error in fulfilling the coupling conditions (13)–(14), and looking at the solution as the minimum of this functional, constrained by the constitutive equations on the 3D and 1D domains:

$$\min_{\overline{\phi},\hat{\psi}} J = \frac{1}{2}\left(\|\gamma_{_\Gamma} u(\overline{\phi},\hat{\psi}) - \mathcal{E}_{_\Gamma}\hat{\psi}\|^2_{\mathcal{H}^{\Gamma}} + \|\gamma_{_\Gamma}\mathcal{E}_{_\Sigma}\hat{u}(\overline{\phi},\hat{\psi}) - \mathcal{E}_{_\Gamma}\hat{\psi}\|^2_{\mathcal{H}^{\Gamma}} \right), \tag{15}$$

such that, for $\check{v}, \hat{\psi} \in \hat{V}$: $\gamma_{\Gamma_i} v = \mathcal{E}_\Gamma \check{v}$ and $\psi = \mathcal{E}_\Gamma \hat{\psi}$:

$$(K\nabla u, \nabla v)_D + \alpha(|\Gamma|\check{u}, \check{v})_\Lambda - \left\langle |\Gamma|\overline{\phi}, \check{v} \right\rangle_{\hat{V}',\hat{V}} = (f, v)_D + \alpha(|\Gamma|\hat{\psi}, \check{v})_\Lambda \quad \forall v \in V_D, \tag{16}$$

$$\left(\tilde{K}|\Sigma|\frac{d\hat{u}}{ds}, \frac{d\hat{v}}{ds}\right)_\Lambda + \hat{\alpha}(|\Gamma|\hat{u}, \hat{v})_\Lambda + \left\langle |\Gamma|\overline{\phi}, \hat{v} \right\rangle_{\hat{V}',\hat{V}} = (|\Sigma|\overline{\overline{g}}, \hat{v})_\Lambda + \hat{\alpha}(|\Gamma|\hat{\psi}, \hat{v})_\Lambda \quad \forall \hat{v} \in \hat{V}, \tag{17}$$

being $\overline{\overline{g}}(s) = \frac{1}{|\Sigma(s)|}\int_{\Sigma(s)} g \, d\sigma$. The terms multiplied by coefficients α and $\hat{\alpha}$ in the constraint equations. (16)–(17) represent a consistent correction, as at the minimum $\check{u} = \hat{u} = \hat{\psi}$. However this correction allows to have well posed problems on each sub-domain independently from the prescribed boundary conditions, provided that $\alpha, \hat{\alpha} > 0$. This is particularly relevant, as one of the key advantages of the proposed approach is to provide a methodology ready for domain decomposition on non conforming meshes. In addition, the discrete problem deriving from the optimization formulation is well posed without requiring the introduction of complex stabilization terms. The above formulation can be extended to accommodate multiple intersecting segments and different couplings between the 3D and 1D domain. The interested reader is referred to the previous works on the subject for further details [3,20,24].

4. Discrete problem

Let us briefly recall here the discrete formulation of problem (15)–(17), in the simplified case of a single inclusion. It is to remark that this is formally identical to the one already described in [3], also for the general case of multiple intersecting 1D domains. Indeed, the focus of the present work is on the application of the XFEM, which does not affect the structure of the discrete system. The choice of the enrichment function and of the quadrature formulas, which are the main novelty content of this work, are thoroughly discussed in the next sections.

As the inclusion is reduced to the centerline Λ, we extend the domain D to cover to the whole Ω. Then we build a mesh $\mathcal{T}$ on Ω made of N_τ tetrahedral elements τ_j, i.e. $\mathcal{T} = \bigcup_{j=1}^{N_\tau} \tau_j$, whose position in space is independent from the position of the 1D domain Λ. On this mesh we choose a set of finite element basis functions $\{\varphi_i\}_{i=1,\dots,N}$, such that the discrete counterpart of unknown u is $U = \sum_{i=1}^{N} U_i\varphi_i$. We proceed similarly for variables $\hat{u}$, $\bar{\phi}$ and $\hat{\psi}$, by first defining on Λ three independent meshes and basis functions sets: mesh $\hat{\mathcal{T}}$ and functions $\{\hat{\varphi}_i\}_{i=1,\dots,\hat{N}}$ for $\hat{u}$, mesh τ^ϕ and functions $\{\theta_i\}_{i=1,\dots,N^\phi}$ for $\bar{\phi}$, and mesh τ^ψ and functions $\{\eta_i\}_{i=1,\dots,N^\psi}$ for $\hat{\psi}$, ending up with the following discrete counterparts for the three variables, defined respectively as:

$$\hat{U} = \sum_{i=1}^{\hat{N}} \hat{U}_i\hat{\varphi}_i, \quad \boldsymbol{\Phi} = \sum_{i=1}^{N^\phi} \boldsymbol{\Phi}_i\theta_i, \quad \boldsymbol{\Psi} = \sum_{i=1}^{N^\psi} \boldsymbol{\Psi}_i\eta_i.$$

The discrete problem is obtained by replacing the above definitions in Eqs. (16)–(17). The discrete functional is then defined as follows:

$$J_\delta = \frac{1}{2}\left(\|U_{|_\Lambda} - \boldsymbol{\Psi}\|^2_{L^2(\Lambda)} + \|\hat{U} - \boldsymbol{\Psi}\|^2_{L^2(\Lambda)}\right),$$

i.e. exploiting the regularity of the discrete variables to directly compute the restriction on Λ of U and using the L^2-norm to compute the coupling mismatch. Then we collect the integrals of the basis functions into the matrices:

$$\boldsymbol{A} \in \mathbb{R}^{N\times N} \text{ s.t. } (A)_{kl} = \int_\Omega \boldsymbol{K}\nabla\varphi_k\nabla\varphi_l \, d\omega + \alpha\int_\Lambda |\Gamma(s)|\varphi_{k|_\Lambda}\varphi_{l|_\Lambda} ds,$$

$$\hat{\boldsymbol{A}} \in \mathbb{R}^{\hat{N}\times\hat{N}} \text{ s.t. } (\hat{A})_{kl} = \int_\Lambda \tilde{\boldsymbol{K}}|\Sigma(s)|\frac{d\hat{\varphi}_k}{ds}\frac{d\hat{\varphi}_l}{ds} \, ds + \hat{\alpha}\int_\Lambda |\Gamma(s)|\hat{\varphi}_k\hat{\varphi}_l \, ds,$$

$$\boldsymbol{B} \in \mathbb{R}^{N\times N^\phi} \text{ s.t. } (\boldsymbol{B})_{kl} = \int_\Lambda |\Gamma(s)|\varphi_{k|_\Lambda}\theta_l \, ds,$$

$$\hat{\boldsymbol{B}} \in \mathbb{R}^{\hat{N}\times N^\phi} \text{ s.t. } (\hat{B})_{kl} = \int_\Lambda |\Gamma(s)|\hat{\varphi}_k \, \theta_l \, ds,$$

$$\boldsymbol{C}^\alpha \in \mathbb{R}^{N\times N^\psi} \text{ s.t. } (C^\alpha)_{kl} = \alpha\int_\Lambda |\Gamma(s)|\varphi_{k|_\Lambda}\eta_l \, ds,$$

$$\hat{\boldsymbol{C}}^\alpha \in \mathbb{R}^{\hat{N}\times N^\psi} \text{ s.t. } (\hat{C}^\alpha)_{kl} = \hat{\alpha}\int_\Lambda |\Gamma(s)|\hat{\varphi}_k \, \eta_{i,l} \, ds,$$

and vectors

$$f \in \mathbb{R}^N \text{ s.t. } f_k = \int_\Omega f\varphi_k \, d\omega,$$

$$g \in \mathbb{R}^{\hat{N}} \text{ s.t. } (g)_k = \int_\Lambda |\Sigma(s)|\overline{\overline{g}} \, \hat{\varphi}_k \, ds.$$

We end up in the following form of the constraints:

$$\boldsymbol{A}U - \boldsymbol{B}\boldsymbol{\Phi} - \boldsymbol{C}^\alpha\boldsymbol{\Psi} = f, \tag{18}$$

$$\hat{\boldsymbol{A}}\hat{U} + \hat{\boldsymbol{B}}\boldsymbol{\Phi} - \hat{\boldsymbol{C}}^\alpha\boldsymbol{\Psi} = g, \tag{19}$$

where, with a notation overload, we denoted the array of degrees of freedom with the same symbol of the corresponding discrete function. We proceed similarly for the functional, which, after defining:

$$\boldsymbol{G} \in \mathbb{R}^{N\times N} \text{ s.t. } (G)_{kl} = \int_\Lambda \varphi_{k|_\Lambda} \varphi_{l|_\Lambda} ds,$$
$$\hat{\boldsymbol{G}} \in \mathbb{R}^{\hat{N}\times \hat{N}} \text{ s.t. } (\hat{G})_{kl} = \int_\Lambda \hat{\varphi}_k \, \hat{\varphi}_l \, ds,$$
$$\boldsymbol{G}^{\Psi} \in \mathbb{R}^{N^\Psi \times N^\Psi} \text{ s.t. } (G^\Psi)_{kl} = \int_\Lambda \eta_k \, \eta_l \, ds,$$
$$\boldsymbol{C} \in \mathbb{R}^{N\times N^\Psi} \text{ s.t. } (C)_{kl} = \int_\Lambda \varphi_{k|_\Lambda} \eta_l \, ds,$$
$$\hat{\boldsymbol{C}} \in \mathbb{R}^{\hat{N}_i \times N^\Psi} \text{ s.t. } (\hat{C})_{kl} = \int_\Lambda \hat{\varphi}_k \, \eta_l \, ds,$$

reads:

$$J_\delta = \frac{1}{2}\left(U^T \boldsymbol{G} U - U^T \boldsymbol{C}\Psi - \Psi^T \boldsymbol{C}^T U + \hat{U}^T \hat{\boldsymbol{G}} \hat{U} - \hat{U}^T \hat{\boldsymbol{C}} \Psi - \Psi^T \hat{\boldsymbol{C}}^T \hat{U} + 2\Psi^T \boldsymbol{G}^\Psi \Psi\right). \tag{20}$$

The discrete problem can be written as:

$$\begin{aligned} &\min_{(\Phi,\Psi)} J_\delta(\Phi, \Psi), \\ &\text{subject to (18)–(19).} \end{aligned} \tag{21}$$

If we introduce the following matrices:

$$\mathcal{G} = \begin{bmatrix} \boldsymbol{G} & 0 \\ 0 & \hat{\boldsymbol{G}} \end{bmatrix}, \quad \mathcal{A} = \begin{bmatrix} \boldsymbol{A} & 0 \\ 0 & \hat{\boldsymbol{A}} \end{bmatrix}, \quad \mathcal{B} = \begin{bmatrix} \boldsymbol{B} \\ -\hat{\boldsymbol{B}} \end{bmatrix}, \quad \mathcal{C} = \begin{bmatrix} \boldsymbol{C} \\ \hat{\boldsymbol{C}} \end{bmatrix}, \quad \mathcal{C}^\alpha = \begin{bmatrix} \boldsymbol{C}^\alpha \\ \hat{\boldsymbol{C}}^\alpha \end{bmatrix}, \quad \mathcal{F} = \begin{bmatrix} f \\ g \end{bmatrix},$$

first order optimality conditions for Problem (21) can be written as:

$$\begin{bmatrix} \mathcal{G} & \mathbf{0} & -\mathcal{C} & \mathcal{A}^T \\ \mathbf{0} & \mathbf{0} & \mathbf{0} & \mathcal{B}^T \\ -\mathcal{C}^T & \mathbf{0} & 2\boldsymbol{G}^\Psi & (-\mathcal{C}^\alpha)^T \\ \mathcal{A} & \mathcal{B} & -\mathcal{C}^\alpha & \mathbf{0} \end{bmatrix} \begin{bmatrix} W \\ \Phi \\ \Psi \\ -P \end{bmatrix} = \begin{bmatrix} \mathbf{0} \\ \mathbf{0} \\ \mathbf{0} \\ \mathcal{F} \end{bmatrix}, \tag{22}$$

where P is the vector of Lagrange multipliers and $W = \begin{bmatrix} U^T, & \hat{U}^T \end{bmatrix}^T$. For small-size problems, the numerical solution of the optimization problem (21) can be obtained by solving system (22) with a direct solver, as done in [3]. For larger problems the approach proposed in [20,24] is recommended, which fully exploits the domain-decomposition methodology introduced by the optimization approach. We remark that both the mentioned resolution strategies can be used in conjunction with the XFEM based version of the method here proposed without any additional complexity.

5. Application of the XFEM

In the definition of the discrete function U we have denoted by $\{\varphi_k\}_{k=1,\dots,N}$ a generic set of basis functions. We can now better define such basis functions, splitting them into two sets: the set of standard linear Lagrangian basis functions, denoted by $\{\varphi_k^s\}_{k\in\mathcal{I}}$, with $\mathcal{I}$ the set of their DOF indexes, and the set of the enrichment basis functions $\{\varphi_k^e\}_{k\in\mathcal{I}^\star}$, with $\mathcal{I}^\star$ the corresponding set of DOF indexes. The enrichment basis functions are built starting from a global enrichment function and then applying the partition of unity method.

The global enrichment function needs to account for the irregular behavior that is expected for the discrete solution. Our choice of enrichment function follows from the results in [18]. We will denote by $\zeta(\boldsymbol{x})$ the global enrichment function, which is defined in a different way if the inclusion entirely crosses the domain of interest, or if it is embedded in the domain. In this latter case, indeed, the enrichment function also needs to control the shape of the solution around the endpoints of the inclusion. Let us start by considering a single inclusion and let us denote by $d_\ell(\boldsymbol{x})$ the distance of a generic point $\boldsymbol{x}$ from the line ℓ passing through Λ (see again Fig. 1). In case Λ crosses the domain from side to side, we define ζ as:

$$\zeta(\boldsymbol{x}) = \zeta^\natural(\boldsymbol{x}) := \begin{cases} -\log(d_\ell(\boldsymbol{x})) & \text{if } d_\ell(\boldsymbol{x}) > R \\ -\log(R) & \text{if } d_\ell(\boldsymbol{x}) \le R, \end{cases} \tag{23}$$

being R, as before, the radius of the original 3D inclusion Σ.

If the endpoints $\boldsymbol{x}_0$ and $\boldsymbol{x}_S$ of Λ lie inside Ω, we define

$$\zeta(\boldsymbol{x}) = \zeta^\flat(\boldsymbol{x}) = \begin{cases} \log\left(\dfrac{\|\boldsymbol{x}-\boldsymbol{x}_S\| + L + \boldsymbol{\tau}_\Lambda \cdot (\boldsymbol{x}_0 - \boldsymbol{x})}{\|\boldsymbol{x}-\boldsymbol{x}_0\| + \boldsymbol{\tau}_\Lambda \cdot (\boldsymbol{x}_0 - \boldsymbol{x})}\right) & \text{if } d_\ell(\boldsymbol{x}) > R, \\ \log\left(\dfrac{\|\boldsymbol{x}_R-\boldsymbol{x}_S\| + L + \boldsymbol{\tau}_\Lambda \cdot (\boldsymbol{x}_0 - \boldsymbol{x}_R)}{\|\boldsymbol{x}_R-\boldsymbol{x}_0\| + \boldsymbol{\tau}_\Lambda \cdot (\boldsymbol{x}_0 - \boldsymbol{x}_R)}\right) & \text{if } d_\ell(\boldsymbol{x}) \le R \end{cases} \tag{24}$$

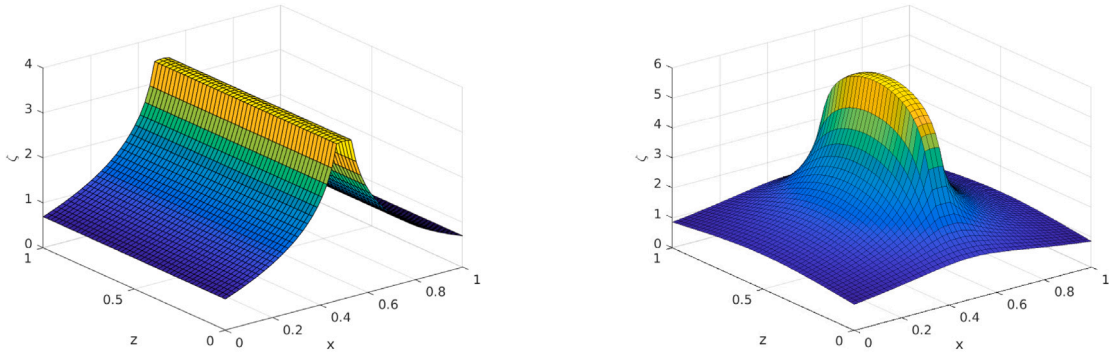

(a) $\zeta = \zeta^{\natural}$ (b) $\zeta = \zeta^{\flat}$

Fig. 2. Enrichment function ζ on a plane containing inclusion centerline. $\Omega = [0,1]^3$, Λ aligned with the z-axis, $R = 10^{-2}$. For $\zeta = \zeta^{\flat}$, Λ extending from $z = 0.2$ to $z = 0.8$.

where $\boldsymbol{\tau}_{\Lambda}$ is the unit tangent vector to Λ, $\boldsymbol{x}_R$ is the projection of $\boldsymbol{x}$ on the infinite cylindrical surface $\mathcal{G}$ containing Γ, $\boldsymbol{x}_0$, $\boldsymbol{x}_S$ are the endpoints of Λ and $L = \|\boldsymbol{x}_S - \boldsymbol{x}_0\|$. Let us observe that

$$\lim_{L\to\infty} \frac{1}{4\pi}\zeta^{\flat}(\boldsymbol{x}) \approx -\frac{1}{2\pi}\zeta^{\natural}(\boldsymbol{x}) \tag{25}$$

is a relation usually used in electromagnetism to approximate the potential of an infinite length line charge. Functions $\zeta^{\natural}(\boldsymbol{x})$ and $\zeta^{\flat}(\boldsymbol{x})$ are shown in Fig. 2 on a plane containing Λ.

Let us now consider a cylinder Δ in Ω with centerline coinciding with Λ and having constant cross-section radius $\rho \geq R$ and let us further denote by $\mathcal{T}_{\Delta}$ the subset of mesh elements in $\mathcal{T}$ having an intersection with the cylinder Δ of non null measure, i.e. $\mathcal{T}_{\Delta} := \{\tau \in \mathcal{T} : |\tau \cap \Delta| > 0\}$. We denote by $\mathcal{J} \subset \mathcal{I}$ the degree of freedom indexes $k \in \mathcal{I}$ such that the support of the standard basis function φ^s_k has a non empty overlap with an element in $\mathcal{T}_{\Delta}$, i.e. $\mathcal{J} := \left\{k \in \mathcal{I} : \exists \tau_j \in \mathcal{T}_{\Delta}, \mathrm{supp}(\varphi^s_k) \cap \tau_j \neq \emptyset\right\}$. We also introduce a continuous ramp function $r_{\mathcal{J}}(\boldsymbol{x})$, equal to one inside $\mathcal{T}_{\Delta}$ and linearly vanishing to zero outside $\mathcal{T}_{\Delta}$, obtained as $r_{\mathcal{J}}(\boldsymbol{x}) := \sum_{k\in\mathcal{J}} \varphi^s_k(\boldsymbol{x})$. For $k \in \mathcal{J}$ we then define $\bar{\varphi}^e_k(\boldsymbol{x}) = \varphi^s_k(\boldsymbol{x})\zeta(\boldsymbol{x})r_{\mathcal{J}}(\boldsymbol{x})$ and finally $\varphi^e_k(\boldsymbol{x}) = \bar{\varphi}^e_k(\boldsymbol{x}) - \bar{\varphi}^e_k(\boldsymbol{x}_k)$, such that the enrichment basis functions are zero-valued in the mesh vertexes $\boldsymbol{x}_k$. Following the XFEM paradigm [21], the effect of the enrichment is local, in a neighborhood of the 1D domain Λ, depending on the chosen value of ρ.

The extension to the case of multiple inclusions is quite straightforward, by simply using the superposition effect. Let us consider $\mathcal{L}$ inclusions Λ_i, and, for each inclusion, let us define a cylinder Δ_i with a centerline coinciding with Λ_i and radius $\rho_i > R_i$, being R_i the radius of the 3D inclusion Σ_i. We then define

$$\mathcal{T}^i_{\Delta} := \left\{\tau \in \mathcal{T} : |\tau \cap \Delta_i| > 0\right\}$$

and

$$\mathcal{J}_i := \left\{k \in \mathcal{I} : \exists \tau_j \in \mathcal{T}^i_{\Delta}, \mathrm{supp}(\varphi^s_k) \cap \tau_j \neq \emptyset\right\}.$$

A different enrichment function is defined for each inclusion, namely

$$\varphi^{e,i}_k(\boldsymbol{x}) = \varphi^s_k(\boldsymbol{x})\zeta_i(\boldsymbol{x})r^i_{\mathcal{J}}(\boldsymbol{x}),$$

with $r^i_{\mathcal{J}}(\boldsymbol{x}) := \sum_{k\in\mathcal{J}_i} \varphi^s_k(\boldsymbol{x})$ and $\zeta_i(\boldsymbol{x})$ defined as in (23) or (24) depending on Λ_i. The discrete approximation of the unknown u is then defined as:

$$U = \sum_{k\in\mathcal{I}} U^s_k \varphi^s_k(\boldsymbol{x}) + \sum_{i=1}^{\mathcal{L}} \sum_{k\in\mathcal{J}_i} U^{e,i}_k \left(\varphi^{e,i}_k(\boldsymbol{x})\right).$$

In practice, the unknowns and the corresponding basis functions are numbered consecutively, giving N total unknowns.

Please note that the case of intersecting inclusions is contained in the above presentation, as we can simply split the intersecting centerlines into sub-segments meeting in one of their endpoints.

In complex configurations, with several inclusions, strategies might be required to avoid the presence of nearly linearly dependent enrichment basis functions or the presence of small intersections between a mesh element and the enrichment region. Details can be found in [21] and references therein. Alternatives are proposed in [25–29].

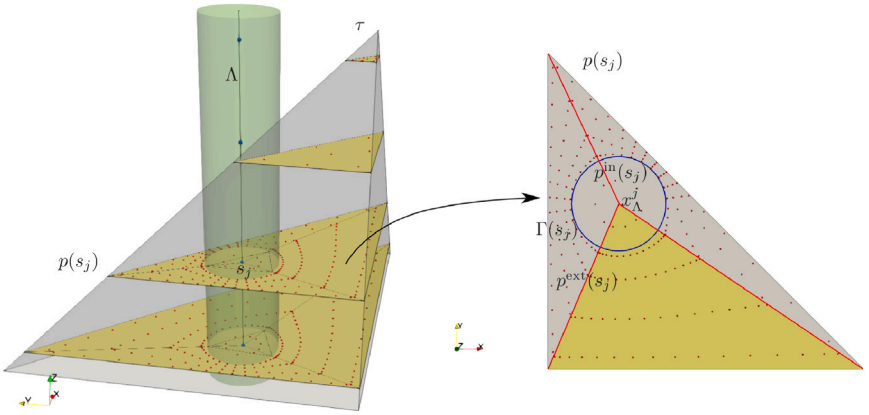

Fig. 3. Description of numerical integration strategy.

Table 1
Numerical quadrature errors for different numbers of integration points.

n_Λ	$n_\mathfrak{r}$	n_θ	N_{pt}	error - $R = 0.1$	error - $R = 0.3$
1	3	5	33	6.94e−05	4.28e−06
1	4	7	59	9.85e−08	2.97e−09
1	6	9	111	6.45e−12	1.75e−12
1	8	12	195	4.57e−16	1.67e−16

6. Numerical integration

A key aspect for the successful application of the XFEM lies in the numerical quadrature of the enrichment basis functions. Given the irregular behavior of such functions, customized strategies need to be adapted, often relying on a sub-division of the three-dimensional domain conforming to the interfaces. Here, the devised approach exploits the known behavior of function $\zeta(\boldsymbol{x})$ and is capable of correctly capturing the curvilinear boundary of the interface. Let us start with the case of an isolated inclusion. With reference Fig. 3, let us consider a tetrahedron $\tau \in \mathcal{T}$, intersected by one inclusion Λ with radius R. Let us denote by $s_{v_0} \geq s_{v_1} \geq s_{v_2} \geq s_{v_3}$ the curvilinear abscissas of the projections on Λ of the four vertexes of τ. We remark that it is possible that some of these projection points coincide, when Λ is orthogonal to one of the faces of the element, as it is the case of Fig. 3. Then, considering a generic enrichment φ^e we have:

$$\int_\tau \varphi^e(\boldsymbol{x})\mathrm{d}\boldsymbol{x} = \sum_{t=0}^{2} \int_{s_{v_t}}^{s_{v_{t+1}}} \left(\int_{p(s)} \varphi^e(\boldsymbol{x})\mathrm{d}\sigma \right) := \sum_{t=0}^{2} \int_{s_{v_t}}^{s_{v_{t+1}}} f_\zeta(s)\mathrm{d}s,$$

in which $p(s)$ is the polygonal region given by the intersection of τ with a plane orthogonal to Λ at $s \in [s_{v_0}, s_{v_3}]$. In each interval $\Lambda^t := [s_{v_t}, s_{v_{t+1}}]$, $t = 0, \dots, 2$, the function representing the surface area of $p(s)$ is smooth, and consequently $f_\zeta(s)$ is smooth. A Gaussian 1D quadrature rule with n_Λ nodes can be efficiently adopted to integrate $f_\zeta(s)$ in each Λ^t, requiring the computation of values $f_\zeta(s_j)$ at integration nodes $s_j \in (s_{v_t}, s_{v_{t+1}})$, $j = 1, \dots, n_\Lambda$. The strategy to compute integrals $f_\zeta(s_j) = \int_{p(s_j)} \zeta(\boldsymbol{x})$ on the regions $p(s_j)$, depends instead on the position of $p(s_j)$. Indeed, if $p(s_j)$ does not contain the irregularity interface of function ζ, we adopt standard quadrature. This is the case, for example, of the two top triangular regions in Fig. 3. Whereas, when $p(s_j)$ contains the interface, as in the two bottom triangular regions in Fig. 3, the integration is performed combining the approaches proposed in [30,31], adapted to the present case, and described in the following. Let us denote by $\boldsymbol{x}^j_\Lambda$ the point at the intersection between Λ and the plane containing $p(s_j)$, and let us denote by $\Gamma(s_j)$ the irregularity interface of ζ at s_j. We remark that this actually coincides with the intersection of $p(s_j)$ with the lateral surface of the original 3D inclusion, see Fig. 3, right. Furthermore, let us call $p^{\text{in}}(s_j)$ the portion of $p(s_j)$ inside $\Gamma(s_j)$, and $p^{\text{ext}}(s_j)$ the portion outside $\Gamma(s_j)$. The regions $p^{\text{in}}(s_j)$ and $p^{\text{ext}}(s_j)$ are each covered by triangular regions with one vertex in $\boldsymbol{x}^j_\Lambda$, as illustrated in Fig. 3, right. In this case we have that $\Gamma(s_j)$ is entirely contained in $p(s_j)$, but such covering can also be determined when it is only partially contained. More details are available in [30]. Now we apply a first mapping $t : [x, y] \mapsto [x^\star, y^\star]$ from each triangular region to the reference triangle, with $\boldsymbol{x}^j_\Lambda$ being mapped to the origin of the reference frame $(x^\star, y^\star)$. We remark that, in such reference frame, the portion of $\Gamma(s_j)$ contained in the triangular region is mapped to an ellipse, centered in the origin. Then we apply a rotation $\varrho : [x^\star, y^\star] \mapsto [\tilde{x}, \tilde{y}]$ to align the axis $x^\star y^\star$ with the principal axis of this ellipse, whose equation is $\frac{\tilde{x}^2}{\lambda_1^2} + \frac{\tilde{y}^2}{\lambda_2^2} = R^2$ in the new frame. Finally we introduce a polar transformation $Y : [\mathfrak{r}, \theta] \mapsto [\tilde{x}, \tilde{y}]$, depending on a parameter q and defined as:

$$\begin{cases} \tilde{x} = \lambda_1 R \mathfrak{r}^q \cos\theta \\ \tilde{y} = \lambda_2 R \mathfrak{r}^q \sin\theta. \end{cases}$$

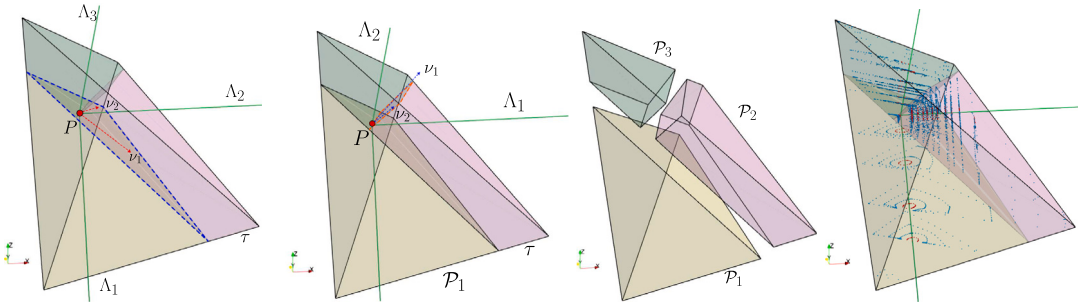

(a) Tetrahedron, split selecting Λ_1 and Λ_2.

(b) Further split selecting Λ_1 and Λ_2.

(c) Tetrahedron split.

(d) Quadrature points generated; red points are inside the inclusions.

Fig. 4. Description of the split strategy.

Now we choose $n_\mathfrak{r}$ Gaussian quadrature nodes along $\mathfrak{r}$ and n_θ nodes along θ which are then mapped back to the physical reference frame (x, y). The three changes of variables allow to correctly integrate the enrichment function close to the curvilinear interface Γ, since the value of q can be chosen to obtain a clustering of the nodes towards the border of the ellipse, where the function has a steep gradient. Higher values of q correspond to a higher clustering. A value $q = 1$ is used for the regions inside Γ, where ζ is constant, whereas a value $q = 3$ is employed for the regions outside Σ. We remark that the above quadrature strategy also applies to general polyhedrons.

As an example, we integrate the function $\zeta^{\natural}(d_\Lambda(\boldsymbol{x}))$ defined in (23) over a unit edge cubic domain $[0, 1]^3$, where Λ coincides with the vertical edge of the cube passing through the origin. We chose this simple geometry to allow for the computation of the exact integral. Two values of R are proposed: $R = 0.1$ and $R = 0.3$. The obtained results are reported Table 1, showing that with the proposed strategy, it is possible to compute the integral from single precision up to machine precision. In the table, N_{pt} represents the total number of quadrature points. The values in columns $n_\mathfrak{r}$ and n_θ refer to the number of quadrature nodes selected in the external regions $p^{\text{ext}}(\cdot)$. Constant values of $n_\mathfrak{r} = 1$ and $n_\theta = 1$ are used for the internal regions $p^{\text{in}}(\cdot)$. Moreover, in this particular case, a single node along Λ is sufficient, considering the simple geometry of the domain and the regularity of the integrated function $f_{\zeta^{\natural}}(s)$.

The above procedure is generalized to the case of multiple inclusions as follows. If multiple non intersecting inclusions pass through a single tetrahedron $\tau \in \mathcal{T}$, or if a single segment ends within a tetrahedron, it is sufficient to split the element into sub-cells such that each sub-cell only contains up to one inclusion, entirely crossing it. Then, we use the quadrature strategy proposed above in cells containing an inclusion, or a classic one, if the considered sub-cell contains no segments.

The case of multiple segments intersecting in point P in a tetrahedral cell $\tau \in \mathcal{T}$ also requires a splitting into sub-cells containing up to a single inclusion (or a portion of a single inclusion). We remark that, in this case, the enrichment function $\zeta = \zeta_i^{\flat}$ needs to be used, as segment endpoints (at least those matching with P) are inside Ω.

We choose to split elements with the following strategy. Let us consider $\mathcal{L} \geq 2$ intersecting segments in $\tau \in \mathcal{T}$, locally numbered as Λ_i, $i = 1, \dots, \mathcal{L}$. We select directions $\boldsymbol{\nu}_1$ and $\boldsymbol{\nu}_2$ as the sum and the external product of the unit tangent vectors of the first two centerlines, respectively, i.e. $\boldsymbol{\nu}_1 = \boldsymbol{\tau}_{\Lambda_1} + \boldsymbol{\tau}_{\Lambda_2}$, and $\boldsymbol{\nu}_2 = \boldsymbol{\tau}_{\Lambda_1} \wedge \boldsymbol{\tau}_{\Lambda_2}$. Then we cut cell τ along the plane containing $\boldsymbol{\nu}_1$ and $\boldsymbol{\nu}_2$ and passing through P. This generates two sub-cells, and the procedure is replicated on each sub-cell. If the sub-cell contains more than two inclusions it is split again along a cutting direction, chosen as above and depending on the local (arbitrary) renumbering of the inclusions in the sub-cell itself. If, on the contrary, a sub-cell contains one or no inclusions, it is left unchanged. The process is recursively applied to each newly generated sub-cell until all sub-cells contain less than 2 inclusions. An example is shown in Fig. 4, for a cell containing three inclusion. The first cut is performed along the plane containing $\boldsymbol{\nu}_1$ and $\boldsymbol{\nu}_2$ in Fig. 4(a) and passing through P, thus generating two sub-cells $\mathcal{P}_1$ and $\mathcal{P}_2$. Cell $\mathcal{P}_1$ contains a single inclusion, and requires no further splitting. Cell $\mathcal{P}_2$, on the contrary, still contains 2 inclusions, locally renumbered as Λ_1 and Λ_2, see Fig. 4(b), and thus it is further split along the plane containing $\boldsymbol{\nu}_1$ and $\boldsymbol{\nu}_2$ passing through P, giving cells $\mathcal{P}_2$ and $\mathcal{P}_3$, see Fig. 4(c). Finally, on each sub-cell we apply the quadrature strategy outlined in Section 6. Fig. 4(d) shows quadrature nodes for the proposed example.

7. Numerical results

The following section is devoted to the presentation of five numerical tests in order to validate and show the effectiveness of the proposed approach. In the following we will denote by N the number of degrees of freedom for variable U, which, for a fixed mesh, can vary according to the radius ρ of the enrichment cylinder Δ. Let us remark that the case $\rho > 0$ corresponds to the optimization based domain decomposition method with the use of the extended finite elements for the 3D variable, while for $\rho = 0$ we end up in the same optimization based approach but with standard finite elements for the 3D variable. For what concerns the 1D variables, piecewise linear continuous basis functions are used for $\hat{U}$ on an equally spaced mesh $\hat{\mathcal{T}}$ and for Ψ on an equally spaced mesh $\mathcal{T}^{\Psi}$, whereas piecewise constant basis functions are used for Φ on an equally spaced mesh $\mathcal{T}^{\phi}$. The refinement level of the 1D meshes

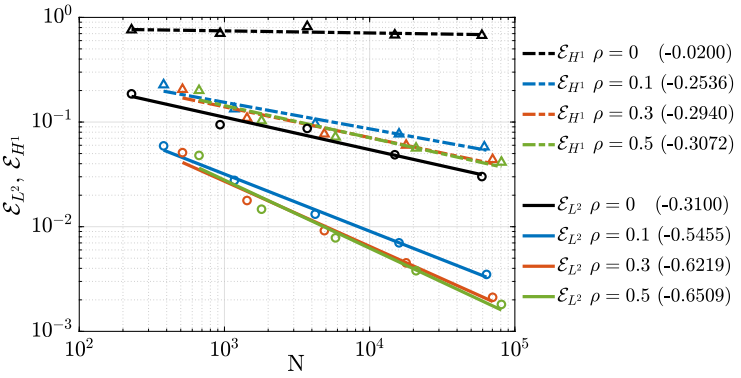

Fig. 5. Test 7.1, trend of the relative errors under mesh refinement. Dashed lines: relative H^1-norm of the error; full lines: relative L^2-norm of the error.

$\hat{\mathcal{T}}$, $\mathcal{T}^\psi$ and $\mathcal{T}^\phi$ is related to the refinement level of the 3D mesh $\mathcal{T}$ and not to the number of degrees of freedom N. More in details, denoted by N_I the number of intersection points between an inclusion Λ and the boundary of the elements in $\mathcal{T}$, mesh $\hat{\mathcal{T}}$ will have $2N_I$ nodes whereas meshes $\mathcal{T}^\psi$ and $\mathcal{T}^\phi$ will count $N_I/2$ nodes. The same is used for each segment in the case of multiple inclusions. The analysis on the behavior of the method with respect to different refinement levels of the various meshes is available in the references, see [3,20]. The solution of the problems in the numerical experiments is obtained by solving system (22) with a direct method.

7.1. 3D problem with singular source term

The first numerical example concerns a 3D problem with a singular source term, and is used to validate the proposed XFEM setting through the comparison with a known analytical solution. Here, we will not solve a coupled 3D–1D problem, but a 3D problem with a known source term on a line. Consequently there is no need of using the optimization based coupling strategy. This example is therefore useful to investigate the effectiveness of the enrichment function shown in Section 5 in describing the expected behavior of the solution on coarse meshes and of the quadrature strategy described in Section 6.

The test considers a cubic domain $\Omega = (-1,1)^3$ with a cylindrical inclusion $\Sigma = \{(x,y,z) : \sqrt{x^2+y^2} < R,\ z \in (-1,1)\}$, of radius $R = 10^{-3}$. The inclusion is dimensionally reduced to a line and we numerically solve problem (16) with $\alpha = 0$, $f = 0$, $K = 1$ and $\overline{\phi} = -\frac{1}{10\pi R}$. The obtained solution is compared to the analytical solution of the original equi-dimensional problem, chosen as:

$$u_{\text{ex}} = \begin{cases} \frac{1}{10\pi}\log(r) & \text{for } r > R \\ \frac{1}{10\pi}\log(R) & \text{for } r \le R \end{cases}$$

with $r = \sqrt{x^2+y^2}$. We can observe that such analytical solution actually matches with the enrichment function $\zeta = \zeta^\natural$, but in the dimensionally reduced problem the flux $\overline{\phi}$ is placed at inclusion centerline and not at the inclusion boundary, thus introducing a modeling error.

The problem is solved on five meshes with maximum element diameter ranging between 0.215 and 0.034. Homogeneous Neumann boundary conditions are prescribed on $\partial\Omega_{\text{n}} = \{(x,y,z) : z = -1 \vee z = 1\}$, whereas Dirichlet boundary conditions, in accordance with the chosen exact solution, are set on $\partial\Omega_{\text{d}} = \partial\Omega \setminus \overline{\partial\Omega_{\text{n}}}$. Convergence trends of the error between the computed and the analytical solution against the total number of degrees of freedom N are reported in Fig. 5 for the L^2 and H^1 relative norms. Four values of the enrichment area are considered, depending on the radius ρ of cylinder Δ (see Section 5): namely $\rho \in \{0, 0.1, 0.3, 0.5\}$. Let us recall that the case $\rho = 0$ corresponds to the application of standard finite elements on a uniformly refined mesh. In this case no convergence in the H^1 norm and a sub-optimal L^2 convergence trend is expected, see [32]. For $\rho > 0$, the convergence trends in Fig. 5 are close to the optimal ones for linear Lagrangian finite elements with regular data, and slightly improve as ρ increases.

Table 2 reports the quadrature parameters employed for the $\rho > 0$ cases: n_Λ, n_τ and n_θ refer to the number of nodes along Λ, τ and θ respectively, as described in Section 6. For n_τ and n_θ we distinguish between the number of quadrature nodes used within the inclusion radius (*in*), where the enrichment is constant, or outside (*out*). Let us recall that the quadrature rule described in Section 6 is used only for elements which are intersected by Σ. The symbol n_Δ, finally, denotes the number of nodes of a standard 3D Gaussian quadrature rule adopted on the tetrahedrons intersecting region Δ but not Σ: in these elements, indeed, we still need to integrate the enrichment functions, but, here, such functions have a continuous gradient. We also remark that the number of quadrature nodes used in a tetrahedron intersected by Σ is typically larger than $n_\Lambda \times n_\tau \times n_\theta$, as it depends on the number of sub intervals Λ^t (see Section 6) used and the number of sub-cells originated by the splitting. Further comments on this aspect are provided in the next examples, in which the same quadrature parameters reported in Table 2 will be considered. The parameters reported in Table 2 are the proposed optimal choice: less nodes yield a decay in convergence trends and an upward shift of the error curves; more nodes lead to a small downward shift of the error curves.

Table 2
Number of quadrature nodes.

n_τ	n_θ	n_Λ	n_Δ
in: 1 *out*: 2	*in*: 1 *out*: 2	2	14

(a) Geometry configuration (b) Mesh for the 3D-3D reference solution (detail)

Fig. 6. Test 7.2: Geometry configuration and detail of the mesh used for the reference solution.

7.2. 3D-1D coupled problem with crossing inclusion

The second numerical example takes into account a 3D–1D coupled problem, and proposes a validation of the XFEM strategy via a comparison with a solution obtained solving with standard FEM the original equi-dimensional problem.

Let us consider a cubic domain $\Omega = (-1, 1)^3$ with a cylindrical inclusion

$$\Sigma = \{(x, y, z) : \sqrt{x^2 + y^2} < R,\ z \in (-1, 1)\},$$

of radius $R = 10^{-2}$ (see Fig. 6(a)). We set $\partial\Omega_d = \{(x, y, z) : z = -1 \vee z = 1\}$ and $\partial\Omega_n = \partial\Omega \setminus \overline{\partial\Omega_d}$, i.e., the Dirichlet boundary consists of the top and bottom faces of the cube, and the Neumann boundary consists of the lateral faces. Problem data are $f = 1$, $g = \overline{\overline{g}} = 0$, $K = 1$ and $\tilde{K} = 10^5$, whereas homogeneous Dirichlet boundary conditions are prescribed on $\partial\Omega_d$ and at the endpoints of Λ, while homogeneous Neumann boundary conditions are set on $\partial\Omega_n$.

To build a reference solution, we solve the original 3D–3D equi dimensional problem with a standard FEM method, on a mesh conforming to the actual interface Γ, which is discretized as the lateral surface of a prism with a 24-edge polygonal base. By standard FEM we actually mean that no domain decomposition is performed, and that a global pressure field U is computed without resorting to an optimization based approach. As shown in Fig. 6(b), the mesh for the reference solution is refined in a region at a distance R from Λ, with elements of maximum diameter of 0.002, while it is coarser outside, where the element maximum diameter is 0.027, resulting in about 3.1×10^5 DOFs.

The corresponding 3D–1D dimensionally reduced problem is solved on a uniformly refined mesh with element maximum diameter of 0.136. We consider the cases $\rho = 0$ and $\rho = 0.01$, corresponding respectively to $N \sim 1.3 \times 10^3$ and $N \sim 1.5 \times 10^3$. Let us recall that the 3D–1D problem is always solved resorting to the optimization based domain decomposition method described in Section 3 and that, for $\rho > 0$, we use the quadrature strategy described in Section 6 with the parameters reported in Table 2.

The solutions obtained on Λ are reported in Fig. 7, along with the trace on Λ of the reference 3D–3D solution. In [3], where the problem was solved only for $\rho = 0$, it was observed that, when $\tilde{K} \gg K$, mesh adaptation is needed close to the inclusion to improve accuracy, since a big jump in the diffusion coefficients produces a 3D solution with a very strong gradient close to the inclusion itself. Here we can see that, a choice of $\rho > 0$ allows to obtain accurate solutions on uniform coarse meshes. Indeed, despite using nearly the same number of DOFs of $\rho = 0$ case, the solution with the XFEM is much closer to the 3D–3D reference solution, with a 4% relative L^2 error on Λ, compared to a 78% error of the $\rho = 0$ case.

7.3. 3D-1D coupled problem with inclusion inside the domain

In this example, we consider the case of an inclusion that is completely embedded into a domain Ω. In particular we choose $\Omega = (-1, 1)^3$ and the original 3D inclusion is

$$\Sigma = \{(x, y, z) : \sqrt{x^2 + y^2} < R,\ z \in (-0.8, 0.5)\},$$

i.e., the endpoints of Λ lie inside Ω, as reported in Fig. 8(a). Problem data are $R = 10^{-2}$, $f = 1$, $K = 1$, $g = \overline{\overline{g}} = 0$, $\tilde{K} = 10^5$ and we impose homogeneous Dirichlet boundary conditions on $\partial\Omega_d = \{(x, y, z) : z = -1 \vee z = 1\}$ and homogeneous Neumann on $\partial\Omega_n = \partial\Omega \setminus \overline{\partial\Omega_d}$ and at the end sections of the inclusion.

As in the previous case, we build a reference solution by solving an equi-dimensional 3D–3D problem with standard finite elements on a mesh conforming to the interface Γ and refined towards the inclusion As reported in Fig. 8(b), this mesh presents

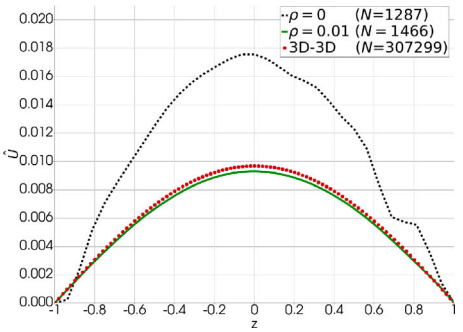

Fig. 7. Test 7.2: solutions on Λ obtained for $\rho = 0$ and $\rho = 0.1$ compared to the trace on Λ of the 3D–3D reference solution.

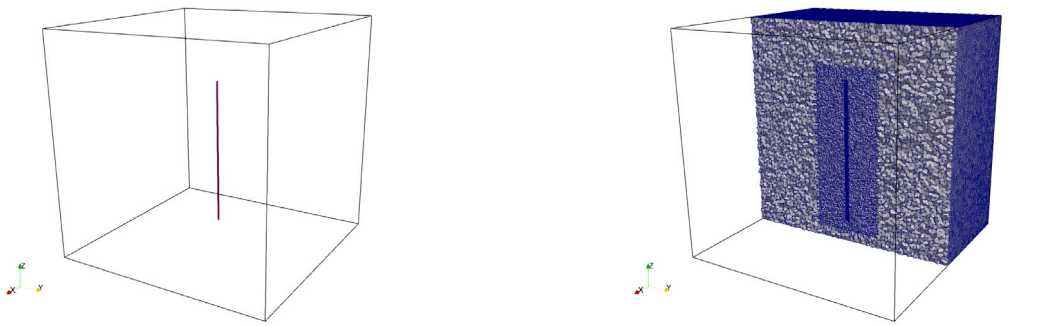

(a) Geometry configuration (b) Mesh for the 3D-3D reference solution

Fig. 8. Test 7.3: geometry configuration and mesh used to compute the reference solution.

three different degrees of refinement. In particular the element maximum diameter is 0.0045 in a region of radius R around Λ, 0.01 outside this region but within a prismatic box $(-0.3, 0.3)^2 \times (-0.9, 0.6)$, and 0.0215 outside the box, resulting in about 4×10^5 DOFs. The 3D–1D reduced problem in instead solved on a uniform mesh, with mesh parameter 0.086, and for $\rho \in \{0, 0.1, 0.3, 0.5, \sqrt{2}\}$, corresponding to a value of N ranging between 4.6×10^3 and 1×10^4.

Fig. 9(a) shows the solutions obtained on Λ. We can observe that for $\rho > 0$, the solutions are much closer to the trace of the reference 3D–3D solution, already for $\rho = 0.1$. Clearly, as ρ increases, the gap with the reference decreases, at the expenses of a larger number of unknowns. Relative errors between the obtained 1D solutions and the trace of the reference solution range between a value of 8×10^{-3}, for $\rho = 0.1$, and 2×10^{-4} for $\rho = \sqrt{2}$, in L^2 norm. The case $\rho = 0$ fails, instead, in providing an equally good representation of the solution, with a 7×10^{-2} relative error on Λ with respect to the reference solution. Indeed, as in the previous test, the large jump in the coefficients between the 3D domain and the 1D inclusion gives a solution with a steep gradient that cannot be correctly reproduced by FEM basis functions on elements with a diameter larger than the radius of the inclusion. We remark that it is not possible to significantly reduce the number of DOFs of the 3D–3D reference solution without affecting its quality. We can then note that choosing $\rho = \sqrt{2}$, i.e. enriching all the basis functions, still gives a number of unknowns about 40 times smaller than the ones required for the equi-dimensional problem.

Fig. 9(b) reports the distribution of the total number of quadrature nodes used in the elements intersected by the inclusion when $\rho > 0$. The maximum number of quadrature nodes in a non-split cell can be easily computed as $3 \times 4 \times n_\Lambda \times n_\tau \times n_\theta = 100$, since 3 is the maximum number of intervals Λ^t in a tetrahedron, 4 is the maximum number of triangular regions on each slice of Fig. 3 and n_Λ, n_τ, and n_θ are the values taken from Table 2, summing the nodes inside and outside Γ. This is confirmed by the values in Fig. 9(b), with the only exception of the two elements containing inclusion endpoints, that are split into sub-cells. Clearly the high number of quadrature nodes represents an additional computational cost. However, in general, this cost is largely offset by the possibility of using less degrees of freedom with respect to approaches that require mesh adaptation. Moreover, the quadrature rule described in Section 6 is only used in elements intersected by Σ, and thus the values of Fig. 9(b) are independent of the chosen value of $\rho > 0$. When the mesh-size is reduced, the number of such elements grows linearly as h^{-1}.

7.4. 3D-1D coupled problem with bifurcated inclusion

Let us now consider the case of a bifurcated inclusion Σ, which can also be seen as the case of multiple inclusions Σ_i whose centerlines Λ_i intersect at one point. In particular, we consider 3 inclusions of radius $R = 10^{-2}$ with centerlines

$$\Lambda_1 = \{(0, 0, z) : z \in (-1.0, -0.1)\}$$

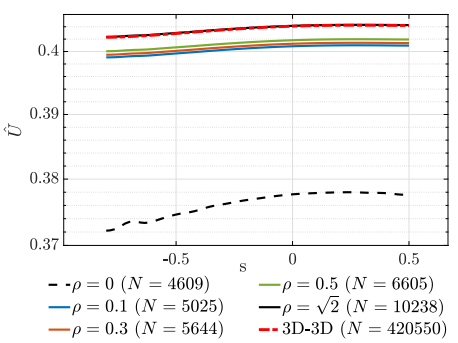

(a) Solutions on Λ

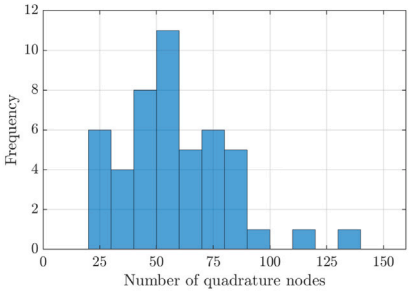

(b) Distribution of quadrature nodes on elements intersected by Σ when $\rho > 0$.

Fig. 9. Test 7.3: solutions on Λ and distribution of the number of quadrature nodes among elements intersected by the bulk inclusion Σ when $\rho > 0$.

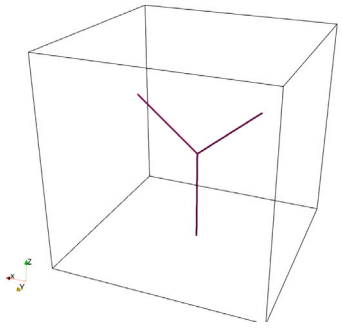

(a) Geometry configuration

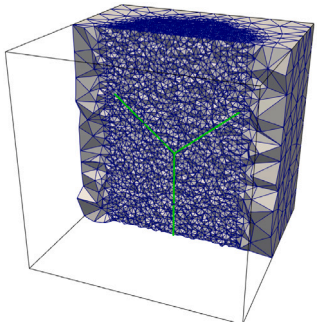

(b) Mesh for the reference solution

Fig. 10. Test 7.4: geometry configuration and mesh used to compute the reference solution.

$$\Lambda_2 = \{(x, 0, z) : x \in (0, 0.6),\ z \in (-0.1, 0.4)\}$$
$$\Lambda_3 = \{(x, 0, z) : x \in (0, -0.6),\ z \in (-0.1, 0.4)\},$$

as shown in Fig. 10(a). Let $\Omega = (-1, 1)^3$ and let us enforce homogeneous Dirichlet boundary conditions on the top and bottom faces of the cube. We also impose a homogeneous Dirichlet boundary condition on the section of the inclusion lying on the bottom face of Ω, and homogeneous Neumann boundary conditions on the sections lying inside Ω. We finally set $f = 1$, $K = 1$, $g = \overline{\overline{g}} = 0$ and $\tilde{K} = 10^5$.

To obtain a reference solution, in this case, we solve the 3D–1D reduced problem with $\rho = 0$, but on a mesh refined within a prism containing the whole inclusion (see Fig. 10(b)). In particular, the prism has a 7-edge polygonal base which can be inscribed in a circle of radius 0.7. Inside the prism the mesh parameter is 0.027, while it is 0.215 outside, resulting in about 4.6×10^4 DOFs. This choice of reference solution is not as reliable as the one of the previous examples, and is motivated by the complexity of generating a mesh conforming to the 3D inclusion for complex geometries, as the ones proposed here and in example 7.5.

The reduced 3D–1D problem is then solved on a uniform mesh with mesh parameter 0.086 and for $\rho \in \{0, 0.1, 0.3, 0.5, \sqrt{2}\}$, corresponding to $N \in [4.6 \times 10^3, 2.2 \times 10^4]$. Let us remark that we are choosing a unique value of ρ for all the inclusions. In the following, when specifying the value of ρ, we will always refer to a solution computed on the uniform mesh.

Fig. 11 shows the solutions for the different values of ρ on the three centerlines Λ_1, Λ_2, Λ_3, along with the corresponding trace of the reference solution. Also in this case we can notice that $\rho > 0$ provides good approximations of the reference solution, whereas the case $\rho = 0$ is less accurate on the uniform mesh.

The distribution of the total number of quadrature nodes used in the elements intersected by Σ when $\rho > 0$ is reported in Fig. 12(a). In this case only four elements exceed 100 quadrature nodes: the two containing the endpoints of the inclusion, the one containing the intersection point and one of its neighbors, which are the elements which actually require splitting. Fig. 12(b) shows a slice of the solution obtained for $\rho = 0.1$ on the yz plane.

Finally, Figs. 13–14 show the solution for $\rho = 0.1$ on planes orthogonal to the z-axis. In the right panels, the reference solution is reported in transparency, to highlight the good matching of the two.

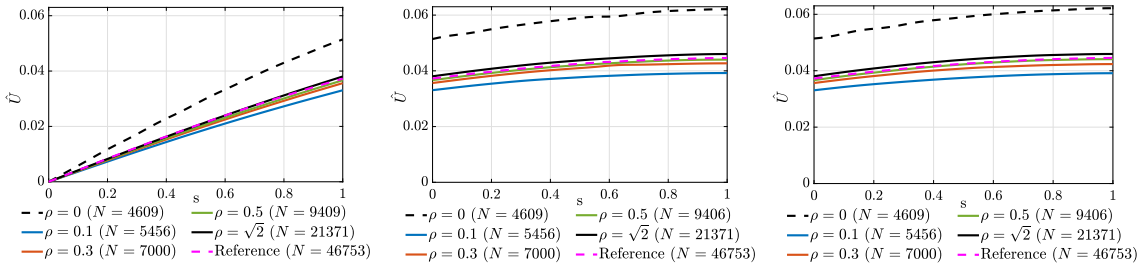

(a) Λ_1 (b) Λ_2 (c) Λ_3

Fig. 11. Test 7.4: solutions on Λ for different values of ρ compared to reference solution.

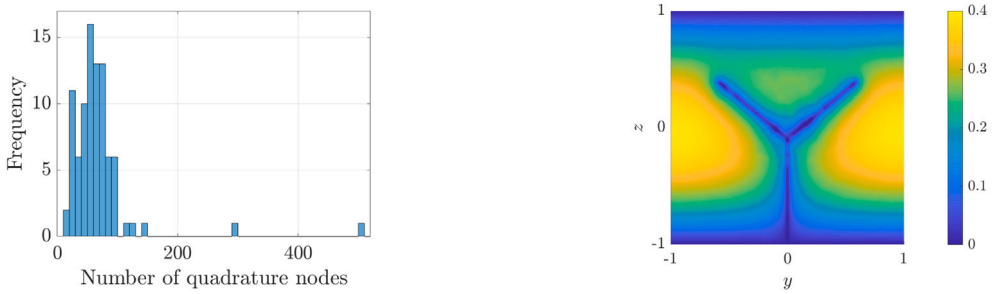

(a) Distribution of quadrature nodes on elements intersected by Σ for $\rho > 0$.

(b) Solution on the yz-plane for $\rho = 0.1$

Fig. 12. Test 7.4: distribution of the number of quadrature nodes among elements intersected by the bulk inclusion Σ when $\rho > 0$ and solution on the yz-plane obtained for $\rho = 0.1$.

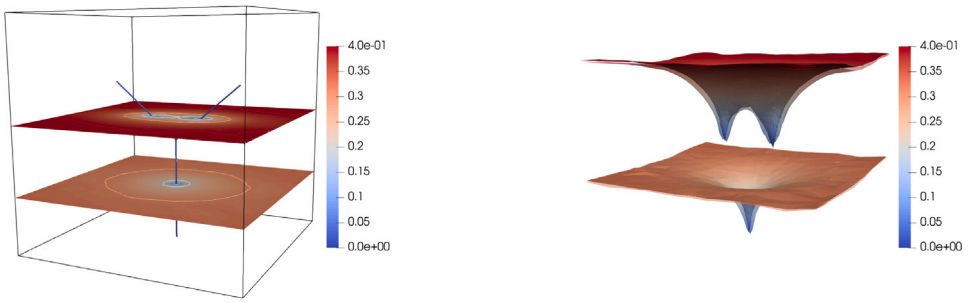

(a) Solution for $\rho = 0.1$ $(N = 5456)$.

(b) Solution obtained for $\rho = 0.1$ $(N = 5456$, opaque) and reference solution $(N = 46753$, transparent)

Fig. 13. Test 7.4: solution on planes orthogonal to the z-axis and located at $z = -0.5$ and $z = 0.1$.

7.5. 3D-1D coupled problems: inclusion with several branches

As a last numerical example, we propose a case with a more realistic inclusion characterized by several branches, as reported in Fig. 15(a) . We assume that the inclusion Σ, which has a constant radius $R = 10^{-2}$, is embedded in a cubic domain $\Omega = (-1, 1)^3$. We chose $f = 0$, $K = 1$, $g = \overline{\overline{g}} = 0$, $\tilde{K} = 10^5$ and we impose homogeneous Neumann boundary conditions on $\partial\Omega_n = \{(x, y, z) : z = -1 \vee z = 1\}$ and homogeneous Dirichlet on $\partial\Omega_d = \partial\Omega \setminus \partial\Omega_n$. For whats concerns the inclusion end sections, we prescribe a Dirichlet boundary condition equal to one at the section lying on the bottom face of the cube, while homogeneous Neumann conditions are prescribed at the dead ends.

As for the previous test case, we build a reference solution by solving the 3D–1D reduced problem with $\rho = 0$ on a mesh refined in a prism containing the inclusion. In this case we consider a prism with a 7-edge polygonal base which can be inscribed in a circle of radius 0.6. Inside the prism we consider a mesh parameter of 0.027, while outside of 0.215, resulting in $N \sim 4.3 \times 10^4$ (see Fig. 15(b)).

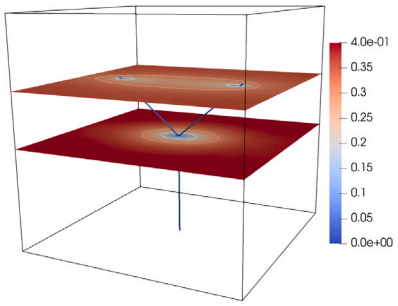

(a) Solution for $\rho = 0.1$ ($N = 5456$).

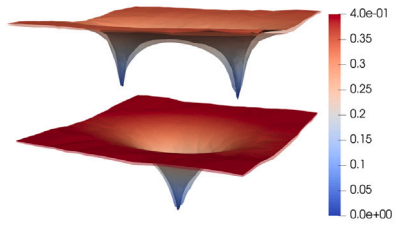

(b) Solution obtained for $\rho = 0.1$ ($N = 5456$, opaque) and reference solution ($N = 46753$, transparent)

Fig. 14. Test 7.4: solution on planes orthogonal to the z-axis and passing through the bifurcation point and close to the two tips.

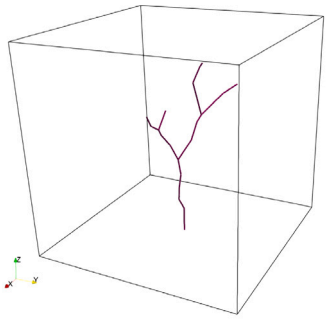

(a) Geometry configuration

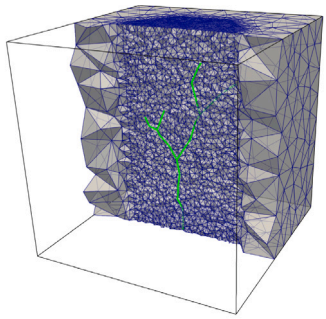

(b) Refined mesh for the reference solution

Fig. 15. Test 7.5: geometry configuration and mesh used to compute the reference solution.

The 3D–1D reduced problem is solved on a uniform mesh of parameter 0.086 with $\rho = 0$ and $\rho = 0.1$, resulting in $N \sim 3.3 \times 10^3$ and $N \sim 4.6 \times 10^3$ respectively. Also in this case, if the value of ρ is specified, we will always refer to a solution computed on the uniform mesh.

The distribution of the number of quadrature nodes among the elements cut by Σ when $\rho > 0$ is reported in Fig. 16, using again the quadrature parameters reported in Table 2. Given the higher number of branches with respect to the previous test cases, the elements needing a high order quadrature formula are slightly more. However, let us remark that only the 0.1% of the total number of elements in the mesh presents more than 100 quadrature nodes. These are the tetrahedrons containing the points in which the network changes direction, the bifurcation points or the dead-ends. Further, only the 0.5% of the total number of elements is cut by at least one tubular inclusion, so that the number of elements in which the quadrature strategy of Section 6 is applied is very small compared to the total number of elements. This overhead is largely offset by the fact that the application of the XFEM avoids the cost of building meshes conforming to the inclusions, or refined near the inclusions.

Fig. 17(a) shows the solutions obtained for $\rho = 0$ and $\rho = 0.1$ on a plane orthogonal to the z-axis and located at $z = 0$. As expected, due to the non conformity of the chosen coarse mesh, standard finite element basis functions ($\rho = 0$) are not able to capture the steep gradient close to the inclusion. Only by refining the mesh it is possible to reproduce the solution obtained for $\rho = 0.1$. This is shown in Fig. 17(b), where a good agreement between the solution obtained with $\rho = 0.1$ and the reference solution can be observed. We recall that the reference solution for this case is a solution computed with $\rho = 0$ on a strongly refined mesh.

Finally, Fig. 18 reports the solution obtained for $\rho = 0.1$ on three different sections of Ω orthogonal to the z-axis (Fig. 18(a)) and on a cylindrical surface parallel to the z-axis itself (Fig. 18(b)).

8. Conclusions

The present work presented an XFEM based implementation of a PDE-constrained optimization method for 3D–1D coupled problems. Suitable enrichment functions have been proposed to tackle problems with thin inclusions in very general cases: inclusions can have arbitrary orientations, form intersections or end inside the domain. A suitable quadrature rule has been introduced to numerically integrate the irregular enrichment functions on general polyhedral cells. The quadrature strategy uses the property of the enrichment functions of being regular in a direction tangential to inclusion centerline, and irregular, with a discontinuous gradient, on planes orthogonal to the centerline. Several numerical tests are proposed to show the effectiveness of the method in capturing the expected behavior of the solution also on meshes characterized by a maximum element diameter much larger than

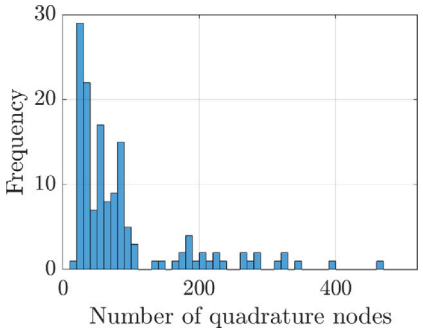

Fig. 16. Test 7.5: distribution of the number of quadrature nodes among the elements intersected by the bulk inclusion Σ when $\rho > 0$.

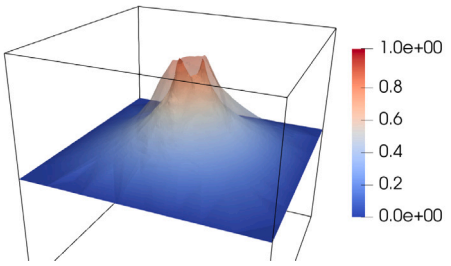

(a) Solution obtained for $\rho = 0$ (transparent, $N = 3331$) and for $\rho = 0.1$ (opaque, $N = 4574$).

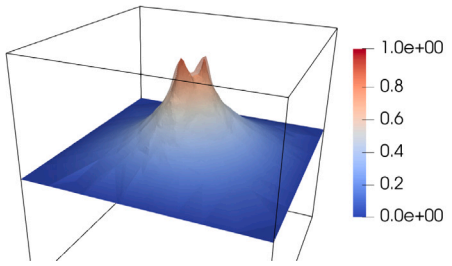

(b) Reference solution (transparent, $N = 43156$) and solution for $\rho = 0.1$ (opaque, $N = 4574$).

Fig. 17. Test 7.5: Solutions on a plane orthogonal to the z-axis and located at $z = 0$.

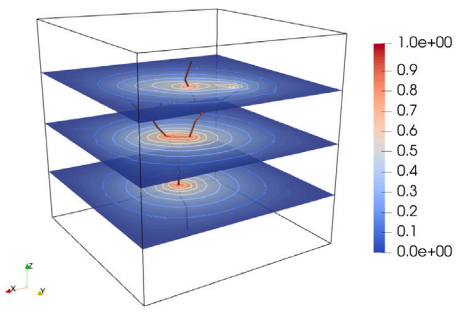

(a) Solution for $\rho = 0.1$ on sections orthogonal to the z-axis.

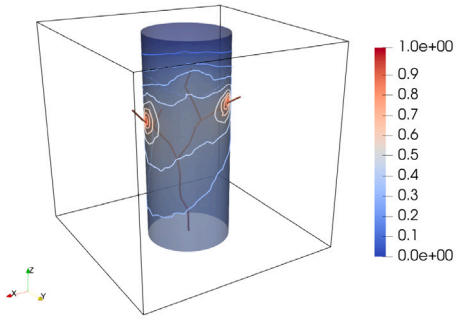

(b) Solution for $\rho = 0.1$ on a cylindrical surface of radius 0.4 and parallel to the z-axis.

Fig. 18. Test 7.5: Solution obtained for $\rho = 0.1$ on three different sections orthogonal to the z-axis and on a cylindrical surface parallel to the z-axis.

the radius of the inclusion. A validation of the methodology is also performed through the comparison with an available analytical solution, or with solutions obtained on adapted meshes. In realistic applications, especially when continuity is imposed at the interface, domain decomposition strategies may become mandatory, also allowing the use of non conforming meshes. The proposed approach enables to take full advantage of such mesh non conformity, avoiding mesh refinement in the vicinity of the inclusions. Moreover, it can be readily used in conjunction with the matrix-free iterative solver discussed in [24] and with different interface conditions, such as filtration-like conditions, thus allowing to simulate a large variety of problems in complex domains.

CRediT authorship contribution statement

Denise Grappein: Writing – review & editing, Writing – original draft, Software, Methodology, Formal analysis, Conceptualization. **Stefano Scialò:** Writing – review & editing, Writing – original draft, Software, Methodology, Funding acquisition, Formal analysis, Conceptualization. **Fabio Vicini:** Writing – review & editing, Writing – original draft, Software, Methodology, Formal analysis, Conceptualization.

Declaration of competing interest

The authors declare that they have no known competing financial interests or personal relationships that could have appeared to influence the work reported in this paper.

Data availability

Data will be made available on request.

Acknowledgments

This publication is part of the project NODES which has received funding from the MUR-M4C2 1.5 of PNRR with grant agreement no. ECS00000036. Authors also acknowledge financial support from INdAM-GNCS.

References

[1] T. Köppl, E. Vidotto, B. Wohlmuth, P. Zunino, Mathematical modeling, analysis and numerical approximation of second-order elliptic problems with inclusions, Math. Models Methods Appl. Sci. 28 (05) (2018) 953–978, http://dx.doi.org/10.1142/S0218202518500252.
[2] F. Laurino, P. Zunino, Derivation and analysis of coupled PDEs on manifolds with high dimensionality gap arising from topological model reduction, ESAIM: M2AN 53 (6) (2019) 2047–2080.
[3] S. Berrone, D. Grappein, S. Scialò, 3D-1D coupling on non conforming meshes via a three–field optimization based domain decomposition, J. Comput. Phys. 448 (2022) 110738, http://dx.doi.org/10.1016/j.jcp.2021.110738.
[4] R. Efrati, D. Givoli, Hybrid 3D-plane finite element modeling for elastodynamics, Finite Elem. Anal. Des. 210 (2022) 103812, http://dx.doi.org/10.1016/j.finel.2022.103812.
[5] N. Mangukiya, S. Yadav, Integrating 1D and 2D hydrodynamic models for semi-arid river basin flood simulation, Int. J. Hydro. Sci. and Tech. (2022) 206–228.
[6] G. Panasenko, Multi-scale Modelling for Structures and Composites, Springer, 2005.
[7] A. Quarteroni, A. Veneziani, C. Vergara, Geometric multiscale modeling of the cardiovascular system, between theory and practice, Comput. Methods Appl. Mech. Engrg. 302 (2016) 193–252, http://dx.doi.org/10.1016/j.cma.2016.01.007.
[8] C. Giverso, P. Ciarletta, Tumour angiogenesis as a chemo-mechanical surface instability, Sci. Rep. 6 (2016) 22610, http://dx.doi.org/10.1038/srep22610.
[9] M.A.J. Chaplain, C. Giverso, T. Lorenzi, L. Preziosi, Derivation and application of effective interface conditions for continuum mechanical models of cell invasion through thin membranes, SIAM J. Appl. Math. 79 (5) (2019) 2011–2031, http://dx.doi.org/10.1137/19M124263X.
[10] I. Steinbrecher, M. Mayr, M. Grill, J. Kremheller, C. Meier, A. Popp, A mortar-type finite element approach for embedding 1D beams into 3D solid volumes, Comput. Mech. 66 (2020) 1377–1398, http://dx.doi.org/10.1007/s00466-020-01907-0.
[11] N. Schröder, M. Javaux, J. Vanderborght, B. Steffen, H. Vereecken, Effect of root water and solute uptake on apparent soil dispersivity: A simulation study, Vadose Zone J. 11 (3) (2012) http://dx.doi.org/10.2136/vzj2012.0009, vzj2012.0009.
[12] T. Koch, K. Heck, N. Schröder, H. Class, R. Helmig, A new simulation framework for soil–root interaction, evaporation, root growth, and solute transport, Vadose Zone J. 17 (1) (2018) 170210, http://dx.doi.org/10.2136/vzj2017.12.0210.
[13] I.G. Gjerde, K. Kumar, J.M. Nordbotten, Well modelling by means of coupled 1D-3D flow models, in: ECMOR XVI - 16th European Conference on the Mathematics of Oil Recovery, 2018.
[14] D. Notaro, L. Cattaneo, L. Formaggia, A. Scotti, P. Zunino, A mixed finite element method for modeling the fluid exchange between microcirculation and tissue interstitium, in: Advances in Discretization Methods: Discontinuities, Virtual Elements, Fictitious Domain Methods, Springer International Publishing, 2016, pp. 3–25, http://dx.doi.org/10.1007/978-3-319-41246-7_1.
[15] T. Köppl, E. Vidotto, B. Wohlmuth, A 3D-1D coupled blood flow and oxygen transport model to generate microvascular networks, Int. J. Numer. Methods Biomed. Eng. 36 (10) (2020) e3386, http://dx.doi.org/10.1002/cnm.3386.
[16] L. Heltai, A. Caiazzo, Multiscale modeling of vascularized tissues via nonmatching immersed methods, Int. J. Numer. Methods Biomed. Eng. 35 (12) (2019) e3264, http://dx.doi.org/10.1002/cnm.3264.
[17] T. Koch, M. Schneider, R. Helmig, P. Jenny, Modeling tissue perfusion in terms of 1D-3D embedded mixed-dimension coupled problems with distributed sources, J. Comput. Phys. 410 (2020) 109370, http://dx.doi.org/10.1016/j.jcp.2020.109370.
[18] I.G. Gjerde, K. Kumar, J.M. Nordbotten, B. Wohlmuth, Splitting method for elliptic equations with line sources, ESAIM: M2AN 53 (5) (2019) 1715–1739, http://dx.doi.org/10.1051/m2an/2019027.
[19] M. Kuchta, F. Laurino, K.-A. Mardal, P. Zunino, Analysis and approximation of mixed-dimensional PDEs on 3D-1D domains coupled with Lagrange multipliers, SIAM J. Numer. Anal. 59 (1) (2021) 558–582, http://dx.doi.org/10.1137/20M1329664.
[20] S. Berrone, D. Grappein, S. Scialò, A PDE-constrained optimization method for 3D-1D coupled problems with discontinuous solutions, Numer. Algorithms (2023) http://dx.doi.org/10.1007/s11075-023-01579-w.
[21] T.-P. Fries, T. Belytschko, The extended/generalized finite element method: An overview of the method and its applications, Internat. J. Numer. Methods Engrg. 84 (3) (2010) 253–304, http://dx.doi.org/10.1002/nme.2914.
[22] R. Gracie, J.R. Craig, Modelling well leakage in multilayer aquifer systems using the extended finite element method, Finite Elem. Anal. Des. 46 (6) (2010) 504–513, http://dx.doi.org/10.1016/j.finel.2010.01.006.
[23] J. Březina, P. Exner, Extended finite element method in mixed-hybrid model of singular groundwater flow, Math. Comput. Simulation 189 (2021) 207–236, http://dx.doi.org/10.1016/j.matcom.2020.12.018.
[24] S. Berrone, D. Grappein, S. Scialò, F. Vicini, A gradient based resolution strategy for a PDE-constrained optimization approach for 3D-1D coupled problems, Int. J. Geomath. 13 (1) (2022) http://dx.doi.org/10.1007/s13137-021-00192-0.
[25] S. Soghrati, A.M. Aragón, C. Armando Duarte, P.H. Geubelle, An interface-enriched generalized FEM for problems with discontinuous gradient fields, Internat. J. Numer. Methods Engrg. 89 (8) (2012) 991–1008, http://dx.doi.org/10.1002/nme.3273.
[26] A.M. Aragón, A. Simone, The discontinuity-enriched finite element method, Internat. J. Numer. Methods Engrg. 112 (11) (2017) 1589–1613, http://dx.doi.org/10.1002/nme.5570.
[27] I. Asareh, T.-Y. Kim, J.-H. Song, A linear complete extended finite element method for dynamic fracture simulation with non-nodal enrichments, Finite Elem. Anal. Des. 152 (2018) 27–45, http://dx.doi.org/10.1016/j.finel.2018.09.002.
[28] I. Asareh, Y.-C. Yoon, J.-H. Song, A numerical method for dynamic fracture using the extended finite element method with non-nodal enrichment parameters, Int. J. Impact Eng. 121 (2018) 63–76, http://dx.doi.org/10.1016/j.ijimpeng.2018.06.012.

[29] I. Asareh, J.-H. Song, Nonnodal extended finite-element method for crack modeling with four-node quadrilateral elements, J. Eng. Mech. 145 (2019) http://dx.doi.org/10.1061/(ASCE)EM.1943-7889.0001662.
[30] S. Falletta, L. Scuderi, A new boundary element integration strategy for retarded potential boundary integral equations, Appl. Numer. Math. 94 (2015) 106–126, http://dx.doi.org/10.1016/j.apnum.2015.03.009.
[31] G. Monegato, L. Scuderi, Numerical integration of functions with boundary singularities, J. Comput. Appl. Math. 112 (1) (1999) 201–214, http://dx.doi.org/10.1016/S0377-0427(99)00230-7.
[32] R. Scott, Finite element convergence for singular data, Numer. Math. 21 (1973) 317–327, http://dx.doi.org/10.1007/BF01436386.